RSC Advances

PAPER

Cite this: *RSC Adv.*, 2019, **9**, 20009

Three hierarchical porous magnesium borate microspheres: a serial preparation strategy, growth mechanism and excellent adsorption behavior for Congo red†

Rui-Feng Guo,‡ Yan-Qing Ma‡ and Zhi-Hong Liu *

The 3D hierarchical porous $7MgO\cdot2B_2O_3\cdot7H_2O$ (MBH) microspheres were prepared by a phase transformation of chloropinnoite firstly, and anhydrous α-$3MgO\cdot B_2O_3$ (MBA) microspheres were obtained by thermal conversion of $7MgO\cdot2B_2O_3\cdot7H_2O$, and then β-$3MgO\cdot B_2O_3$ (MBB) microspheres were obtained by phase conversion of α-$3MgO\cdot B_2O_3$. All samples were characterized by XRD, FT-IR, TG and SEM. The microsphere nanostructures with a hierarchical porous structure were assembled by nanosheets with a thickness of 20–30 nm, and the growth mechanisms were also proposed. By using N_2 adsorption–desorption, the specific surface areas were measured as 103.62 $m^2\ g^{-1}$ for MBH and 46.10 $m^2\ g^{-1}$ for MBA. They exhibited excellent selective adsorption performance for Congo red (CR) with maximum adsorption capacities of 202.84 and 170.07 mg g^{-1} respectively, and the corresponding adsorption mechanisms were also investigated. The adsorption processes were well fitted with the pseudo-second-order rate equation and Langmuir adsorption model. In addition, the corresponding adsorption thermodynamic parameters were also calculated. It is necessary to highlight that the hierarchical porous microspheres could be considered as promising candidates for removal of CR dye pollutants.

Received 15th May 2019
Accepted 17th June 2019

DOI: 10.1039/c9ra03654g

rsc.li/rsc-advances

Introduction

It is well-known that organic dyes, such as Congo red (CR), Methyl orange (MO), Methylene blue (MB), and Rhodamine B (RB) (Fig. S1†), are highly toxic, potentially carcinogenic and not easily biodegradable, which makes their presence in water bodies a serious threat to the environment, health and safety.[1,2] Hence, the development of strategies that remove dyes from samples of aqueous solutions is of significant interest. Until now, several water treatment technologies have been implemented to remove dyes from wastewater, in which the chemical oxidation, photocatalytic degradation,[2] membrane separation,[3] and biodegradation[4] methods are expensive, complex and easily generate secondary pollutants. Adsorption is the most commonly used method due to its advantages of high efficiency, low cost, no secondary pollution, and simple operation process.[5,6] 3D hierarchical porous materials with ultrahigh surface areas and large pore volumes have been extensively applied in water treatment.[7,8]

Borate is a kind of important functional material because of its unique and rich structure. For example, magnesium borates might be as antiwear and antifriction additives,[9] flame retardant,[10] and nanowhiskers.[11,12] Until now, there were several reports about the preparation of different magnesium borates with hierarchical nanostructures, such as flower-like $Mg_7B_4O_{13}\cdot7H_2O$ prepared *via* surfactant poly(vinyl pyrrolidone) (PVP) assisted precipitation process,[13] $MgBO_2(OH)$ superstructures prepared by ionothermal synthesis method,[14] and $2MgO\cdot B_2O_3\cdot H_2O$ microsphere constructed by nanobelts array prepared by a template-free hydrothermal method.[15] Among them, the adsorption performances for Congo red on $MgBO_2(OH)$ superstructures[14] and $2MgO\cdot B_2O_3\cdot H_2O$ microsphere[15] have also been systematically investigated.

Further developing simple and template free methods for the preparation of hierarchical nanostructures with high surface area and excellent adsorption performance are still a challenging work. This paper first reports the preparation of hierarchical porous $7MgO\cdot2B_2O_3\cdot7H_2O$ microspheres by a phase transformation of double salt chloropinnoite ($2MgO\cdot2B_2O_3\cdot MgCl_2\cdot14H_2O$) which was crystallized out from high-boron-containing concentrated brine in Qinghai Salt Lake, China,[16] and then well-preserved flower-like anhydrous α-

Key Laboratory for Macromolecular Science of Shaanxi Province, School of Chemistry and Chemical Engineering, Shaanxi Normal University, Xi'an 710062, PR China. E-mail: liuzh@snnu.edu.cn; Tel: +86-29-81530805

† Electronic supplementary information (ESI) available. See DOI: 10.1039/c9ra03654g

‡ Both authors contributed equally to this work and should be considered co-first authors.

$3MgO \cdot B_2O_3$ microspheres with high crystallinity were obtained by a thermal conversion of $7MgO \cdot 2B_2O_3 \cdot 7H_2O$ microspheres. Both exhibit excellent adsorption performance for Congo red, which could be used as a promising adsorbent for CR from wastewater.

Experimental

Preparation of hierarchical flower-like $7MgO \cdot 2B_2O_3 \cdot 7H_2O$ microsphere by a phase transformation method

All used chemicals were of analytic reagent grade without further purification. Chloropinnoite was obtained according to the ref. 17.

0.4 g of chloropinnoite was added into a 50 mL Teflon-lined stainless steel autoclave which contains 30 mL of deionized water. After the solution was magnetic stirred for 60 min at room temperature, the autoclave was sealed and placed into an oven at 100 °C for 24 h. After cooling to room temperature, the white precipitates obtained were separated by filtration and washed 3 times with distilled water and absolute ethanol respectively, and then dried at 60 °C for 6 h.

Preparation of hierarchical $3MgO \cdot B_2O_3$ nanostructure by a thermal conversion method

The above prepared MBH was placed in a crucible, which was calcined in a muffle furnace to 700 °C or 900 °C at a heating rate of 2 °C min^{-1} and continuously reaction for 3.5 h. After calcination, the obtained product for α-$3MgO \cdot B_2O_3$ or β-$3MgO \cdot B_2O_3$ was naturally cooled to room temperature and washed 3 times with distilled water and absolute ethanol, and dried at 60 °C for 6 h.

Characterization of prepared samples

All samples were characterized by X-ray diffraction (XRD, Rigaku DMX-2550/PC, operating with Cu K_α radiation (λ = 1.5418 Å) at a scanning rate of 10° min^{-1} in a 2θ range from 5° to 70°), Fourier transform infrared (FT-IR) spectrum (measured on a Tensor27 infrared spectrometer (Bruker) using KBr disks), and thermal analysis (TG-DSC, performing on a TGA/DSC3+, METTLER thermal analyzer under a nitrogen atmosphere with a heating rate of 10 °C min^{-1} over the range from 30 to 800 °C). The morphologies of the samples were observed by field emission scanning electron microscopy (FSEM, SU-8020, Hitachi). The porosity and the Brunauer–Emmett–Teller (BET) specific surface area of samples were measured by the nitrogen adsorption/desorption at 77.3 K by using surface analytical instrument (America Micromeritics ASAP 2460. The sample had been degassed at 120 °C for 6.0 h under vacuum of 10^{-5} bar), and the pore size distribution was evaluated from the N_2 desorption isotherm using the Barrett–Joyner–Halenda (BJH) model. The zeta potentials were measured with a dynamic light scattering instrument (Nano-ZSE, Malvern) at 90°.

Adsorption experiments

Adsorption experiments were conducted at 25 °C. 5 mg of MBH or MBA sample was taken, and added to 20 mL of 20–200 mg L^{-1} CR aqueous solution. After magnetic stirring for different times, the liquid–solid phases were separated by using a centrifuge (12 000 rpm). About 3 mL solution was taken and analyzed by UV-vis spectroscopy (UV-6100S double beam spectrophotometer, Mapada, China). Using a linear calibration curve over 2.5–25 mg L^{-1}, the CR concentration was obtained by the peak of the absorbance band at the wavelength of 499 nm. Moreover, to study the kinetics of adsorption, the adsorption of CR solutions with initial concentration of 35 mg L^{-1} was monitored.

The adsorption capacity q_t (mg g^{-1}) at time t, the equilibrium adsorption capacity q_e (mg g^{-1}) and the removal efficiency Re of CR by MBH or MBA nanostructure were calculated using the following eqn (1)–(3):

$$q_t = \frac{(C_0 - C_t)V}{m} \quad (1)$$

$$q_e = \frac{(C_0 - C_e)V}{m} \quad (2)$$

$$\mathrm{Re} = \frac{C_0 - C_t}{C_0} \times 100\% \quad (3)$$

where C_0, C_e and C_t (mg L^{-1}) represent the original concentration, equilibrium concentration and the concentration of CR at different times during the adsorption process, respectively. V is the volume of the solution (mL), and m (mg) is the mass of the added adsorbent of MBH or MBA nanostructure.

Results and discussion

Characterization of samples

As shown in XRD patterns of the prepared samples (Fig. 1), all the diffraction peaks can be indexed as the JCPDS card no. 19-0754 for $7MgO \cdot 2B_2O_3 \cdot 7H_2O$, JCPDS card no. 33-0858 for α-$3MgO \cdot B_2O_3$, and JCPDS card no. 38-1475 for β-$3MgO \cdot B_2O_3$.

FT-IR spectrum of the MBH (Fig. S2†) exhibits the following absorption bands, which are assigned referring to the literature.[18] 3584 and 3444 cm^{-1} (stretching vibration of O–H), 1637 cm^{-1} (H–O–H bending). 1496 cm^{-1} (asymmetric stretching of B(3)–O), 1273 cm^{-1} (B–O–H in-plane bending mode), 1073 cm^{-1} and 974 cm^{-1} (asymmetric and symmetric stretching of B(4)–O respectively), 562 cm^{-1} (bending mode of B(4)–O). These IR assignments show its structure containing BO_3, BO_4 and B–O–H groups.

Fig. 2 gives the simultaneous TG-DSC curves. TG analysis indicates that there exists a weight loss of 23.68% from 100 °C to 600 °C, which correspond to the loss of 7 water molecules per molecule of $7MgO \cdot 2B_2O_3 \cdot 7H_2O$, and basically consist with the calculated value of 23.01%. In the DSC curve, the endothermic peak at 419.1 °C corresponds to the loss of 7 water molecules and the further decomposition of $7MgO \cdot 2B_2O_3 \cdot 7H_2O$. The exothermic peak at 695.5 °C with no related weight loss corresponds to the recrystallization of formed α-$3MgO \cdot B_2O_3$. The exothermic peak at 845.5 °C corresponds to the phase transformation from α-$3MgO \cdot B_2O_3$ into β-$3MgO \cdot B_2O_3$. This result provides the prepared basis for calcining at 700 °C and 900 °C by thermal conversion method.

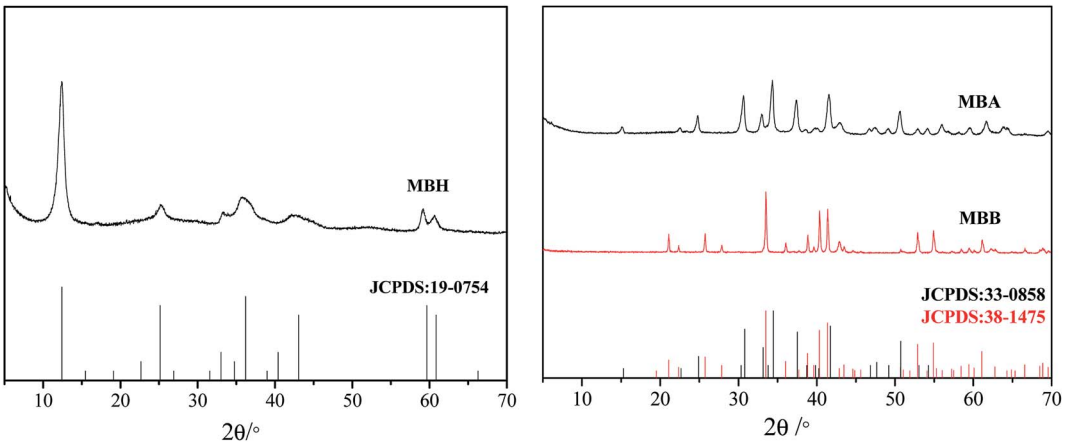

Fig. 1 XRD pattern of prepared MBH, MBA and MBB samples.

The SEM images of samples are shown in Fig. 3. Fig. 3a and b demonstrate that the precursor chloropinnoite exhibits belt shape with different lengths. Fig. 3c shows that the sample MBH exhibits flower-like microsphere with a diameter of ~6 μm, which is assembled by the nanosheets with a thickness of about 20–30 nm as shown in Fig. 3d. Fig. 3e shows that the sample MBA exhibits a similar morphology to MBH, but the constituent unit of microsphere is nanosheet with many holes as seen in high magnification times for SEM (Fig. 3f). From Fig. 3g and h, it can be seen that the sample MBB exhibits a similar morphology to MBA.

The specific surface areas and porous natures of MBH and MBA microspheres

Fig. 4 gives the nitrogen sorption isotherms of the as-prepared samples and their corresponding Barrett–Joyner–Halenda (BJH) pore size distribution. It can be seen from the curves that the adsorption isotherms exhibit type IV and the hysteresis loop of type H3, which indicate the existence of mesopores according to the definition of IUPAC.[19] When the relative pressure (P/P_0) is close to 1, hysteresis loops can be observed, which indicates the existence of macropores (>50 nm). The pore size distribution curves were obtained by using the Halsey equation and the branch calculation of nitrogen desorption isotherms by BJH method. It can be seen from inset of Fig. 4 that there exist a wide pore size distribution. The major peak for the MBH aperture distribution is in the 20.0–40.0 nm, and that for the MBA aperture distribution is in 40.0–60.0 nm, which indicates that there are more mesoporous pores in the MBH microspheres, and there are a few mesoporous and large pores in the MBA nanostructures. In the microsphere structure, the smaller pores might originate from the nanosheets, and the larger pores originate from the gap between the nanosheets of the hierarchical structure. The mesopores and macropores will make the as-obtained hierarchical microspheres with great potential applications.

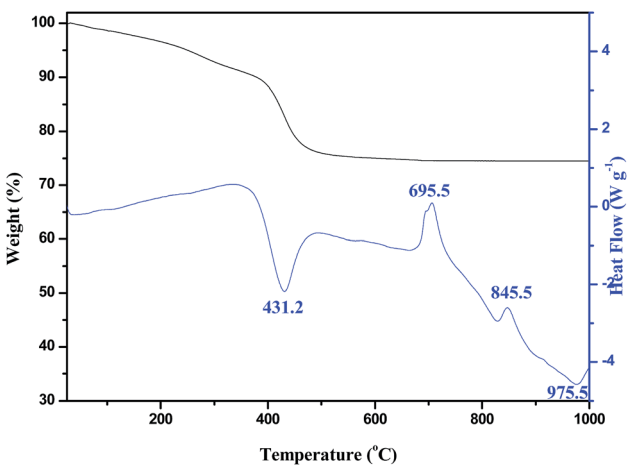

Fig. 2 TG-DSC cures of the prepared MBH sample.

It is well known that the specific surface area (BET) is one of the important indicators for measuring porous materials. The measured BET values of samples are 103.62 $m^2 g^{-1}$ for MBH and 46.10 $m^2 g^{-1}$ for MBA. The pore volumes of microspheres are 0.56 $cm^3 g^{-1}$ for MBH and 0.19 $cm^3 g^{-1}$ for MBA. The average pore sizes are 25.75 nm for MBH and 20.05 nm for MBA. For these parameters, MBA sample has smaller values, which might be resulted from some holes and gaps being blocked due to the calcination of MBH in the process of thermal conversion, although its flower-like shape is well preserved.

With larger BET, the MBH is expected to provide more active sites for adsorption, thus resulting in higher adsorption capacity. The above results confirm that the wider pore size distribution makes these two kinds of special porous microspheres adsorbent have better application prospects in wastewater treatment.

The influence of reaction times on the morphologies of MBH sample

In order to better understand the formation mechanism of the MBH microsphere, the influence of hydrothermal treatment times on the morphologies was investigated. The SEM images of as-prepared samples in different hydrothermal treatment times are shown in Fig. S3.† The time-dependent experimental result shows that nanosheets were formed at 6 h. As the reaction time was extended to 13 h, the rudiment for quarter flower-like sphere was

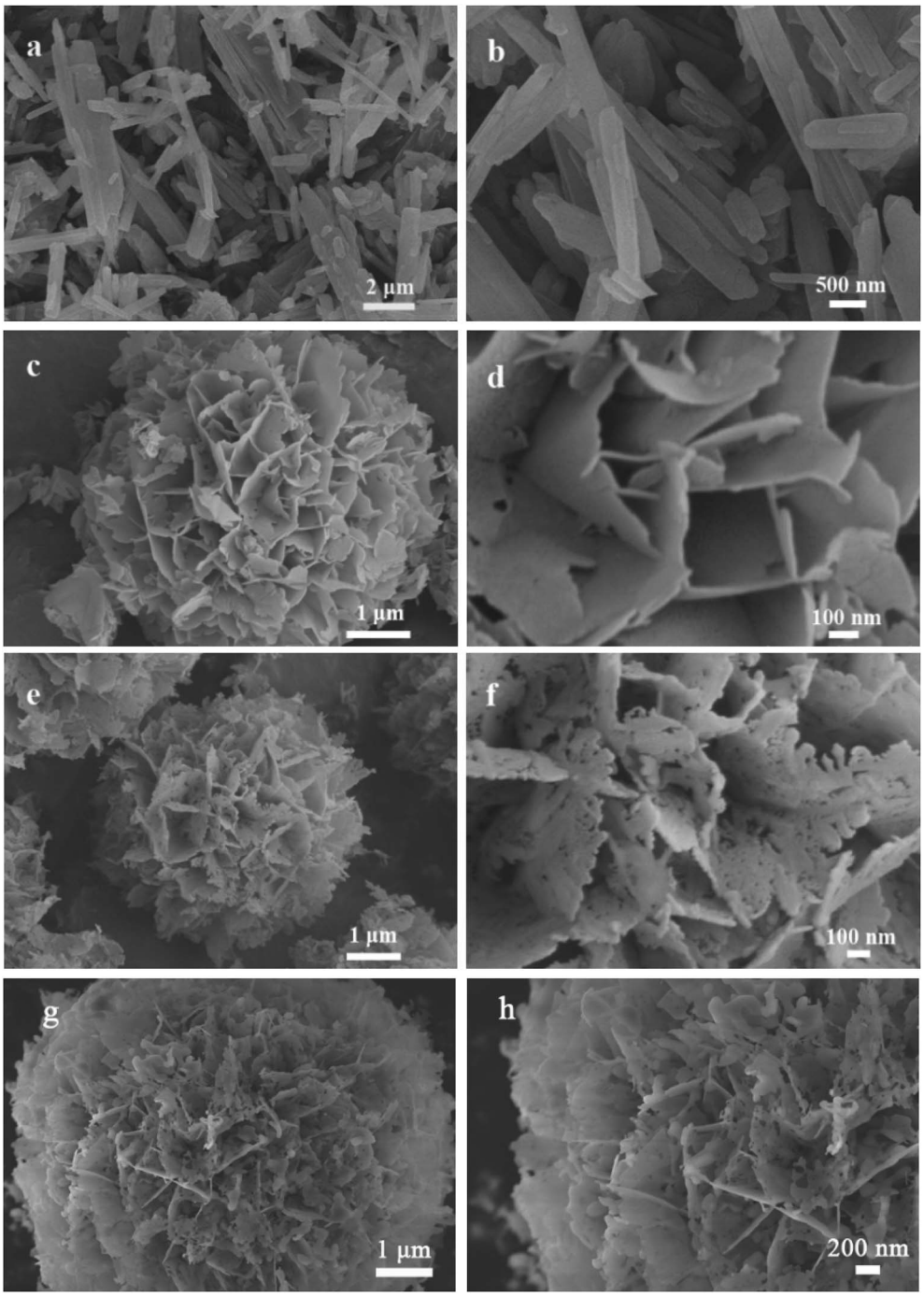

Fig. 3 SEM images of samples: (a and b) chloropinnoite, (c and d) MBH, (e and f) MBA, (g and h) MBB.

formed. When the reaction time reached to 20 h, the incomplete hollow microspheres were formed. When the reaction time further prolong to 24 h, the complete porous microsphere nanostructures assembled from nanosheets were obtained.

The formation mechanism for the flower-like MBH, MBA and MBB microspheres

From the results of influence of different reaction times on the morphologies, the growth process for flower-like microsphere of MBH has been proposed as shown in Scheme 1.

Source material of chloropinnoite was firstly dissolved in large amount of water, then this dilute solution was heated at 100 °C for 24 h under hydrothermal conditions, and MBH nanosheets was formed at 6 h by the phase transformation of chloropinnoite. Subsequently, due to the high surface energy of the MBH nanosheet, these nanosheets spontaneously self-assembled by overlapping mode to form the rudiment for quarter flower-like sphere at 13 h, and incomplete hollow microsphere at 20 h. Finally, as the reaction time prolonging, the complete flower-like microspheres for MBH were formed

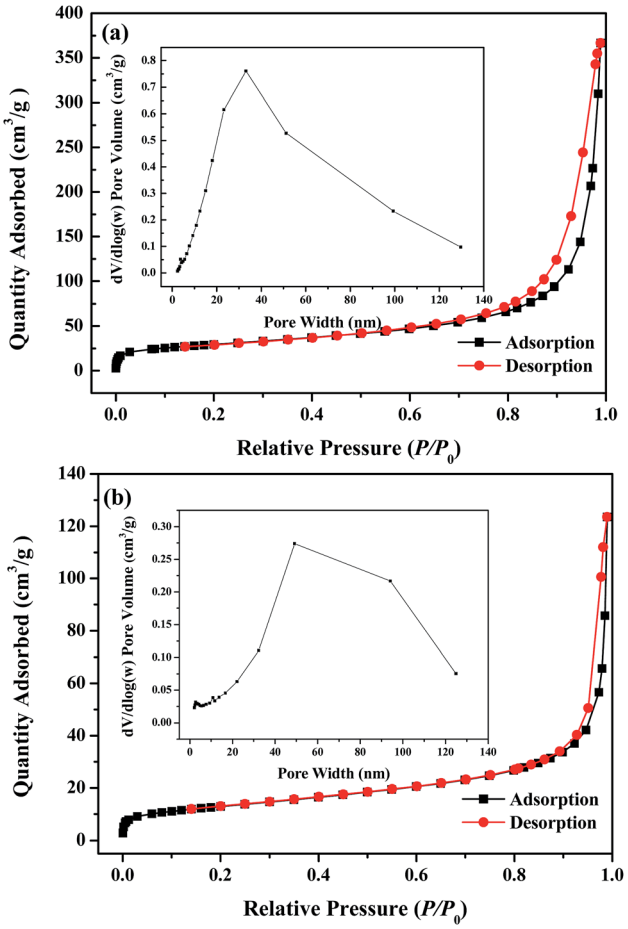

Fig. 4 Nitrogen adsorption–desorption isotherms and corresponding pore diameter distribution profile (inset) of the as-obtained MBH (a) and MBA (b).

due to further growth. It needs to indicate that $7MgO{\cdot}2B_2O_3{\cdot}7H_2O$ was the firstly obtained phase transformation product from chloropinnoite, through various magnesium borates of $2MgO{\cdot}3B_2O_3{\cdot}15H_2O$, $MgO{\cdot}B_2O_3{\cdot}3H_2O$ and $2MgO{\cdot}B_2O_3{\cdot}1$–$2H_2O$ were obtained by this method.[17]

The high crystalline flower-like MBA microspheres construed by nanosheets with many holes were obtained by a thermal conversion of $7MgO{\cdot}2B_2O_3{\cdot}7H_2O$ microspheres at 700 °C, then MBA was phase transformed into MBB at 900 °C. The keeping of microspheres and the existing holes in constituent unit for nanosheet should be related to the very slow heating rate of 2 °C min^{-1}.

The effects of MBH and MBA microspheres on adsorption of different dyes and the corresponding adsorption mechanism

Generally, porous hierarchical nanostructures with high surface areas possess superior adsorption performance. To confirm the utility of two microspheres in water treatments, we used four different organic dyes, Congo red (CR), Methyl orange (MO), Methylene blue (MB), and Rhodamine B (RB), as molecular probes to explore the activity of the adsorbent. 5 mg of MBH or MBA sample was taken, and added to 10 mL of 20 mg L^{-1} organic dye aqueous solution. After adsorbing the different dyes for 3 h with the MBH and MBA adsorbents respectively, the UV-vis absorption spectra of the different organic dyes before and after being absorbed are shown in Fig. S4.† It can be seen that the absorbance has no significant changes in MO and RB, and the absorbance has a slight decrease in MB. But the absorbance has significant changes in CR, which shows that the samples MBH and MBA have a specific selectivity for the adsorption of CR. In addition, the adsorption of CR for sample MBB is slightly weaker than that of sample MBA, which might be resulted from the collapsing of part holes during phase conversion under higher temperature. So, the adsorption of CR for sample MBB was no necessary to investigate. In order to further illustrate specific selectivity for the adsorption of CR, the UV-vis adsorption of mixtures of a cationic dye for RB with CR by MBA was also tested. As shown in Fig. S4(e),† the CR characteristic peak disappear and RB characteristic peak keep no changing after adsorption.

In order to determine the interaction between the adsorbent and CR molecules, zeta potential analysis was used to investigate the surface charge of the sample particles in aqueous solution.[20] The results of zeta potential analysis are shown in Fig. S5.† As can be seen that the potential values of the two adsorbents in the solution are positive, while the potential value of the CR solution is negative, combined with the above adsorption performance, indicating that the interaction between the adsorbent and CR (the anionic dye molecules) may be electrostatic interaction.[21] Hence, CR containing the negatively charged $-SO_3^-$ group would be attracted to the positively

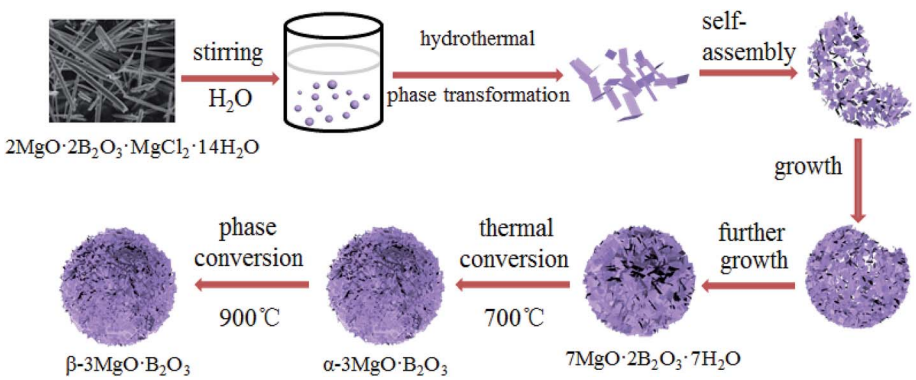

Scheme 1 The formation mechanism for the flower-like MBH, MBA and MBB microspheres.

charged surface of the MBH and MBA samples *via* electrostatic interaction. Though MO is also an anionic dye, its adsorption effect is poor. After comparing the two molecular structures (Fig. S1†), we find that the size of MO molecule is much smaller than that of CR molecule, which might lead to MO molecule penetrating the mesopores and macropores in the MBH microsphere easily. In addition, we also find that there are two $-SO_3^-$ groups and two amino groups ($-NH_2$) in the molecular structure of CR, while there is one $-SO_3^-$ group and no $-NH_2$ group in MO molecular structure. So, there not only exist more electrostatic interaction between CR and MBH/MBA samples, but also exist more hydrogen bonds N–H···O and O–H···N between CR and MBH/MBA samples that contains the hydroxyl group (–OH) on the surface of nanosheet. But both electrostatic interaction and hydrogen bond between MO and MBH/MBA samples are weaker. Both MB and RB are cationic dyes, and the zeta potentials of MBH and MBA samples are both positive, which is not conducive to the adsorption. In addition, the steric hindrance of RB is larger, which is also less favorable for adsorption. Herein, the prepared hierarchical porous flower-like MBH and MBA nanostructures would be used to removal of CR in solution in detail.

Adsorption kinetics

Adsorption kinetics is essential for adsorption research because this process can estimate the adsorption rate and illuminate the mechanism between pollutants and adsorbents. In order to compare the adsorption performance of samples MBH and MBA, we examined the removal efficiency (Re) of MBH and MBA on CR solutions at different time intervals. Fig. 5(A) shows the Re for 20 mL of 35 mg L^{-1} of CR solution after being treated by 10 mg of prepared MBH or MBA nanostructures at different time intervals. It can be seen that the adsorption rates were faster due to the rapid increase in removal efficiency values. Obviously, the Re of sample MBH is higher than that of sample MBA. At the time of adsorption of 60 min, the Re of MBH to CR is about 93%, while the Re of MBA to CR is only 78% under the same conditions. After MBH adsorbed for 120 min, Re was as high as 98.6%. After MBA adsorbed for 300 min, Re was 91.4%. It is obvious that the MBH sample has the better adsorption efficiency, which can be attributed to the fact that the MBH has a larger specific surface area and its unique pore structure, resulting in more active sites. About the decreased adsorption efficiency of MBA, it might be resulted from lower BET value and some unique microstructures being destroyed when calcination of MBH to be prepared MBA.

As a comparison, keeping others conditions unchanged, the effect of contact time on CR removal efficiency by the prepared MBH nanostructure for different initial CR concentrations of 35 mg L^{-1} and 60 mg L^{-1} was also investigated. As showed in Fig. 5(B), the lower the CR concentration, the shorter the time to reach equilibrium, and the higher of the dye removal rate.

To further fully comprehend the inner laws and characteristics of the adsorption process, the pseudo-first-order kinetic models (eqn (4)) and pseudo-second-order kinetic models (eqn (5)) were applied to study the adsorption mechanism.[15,22] The linear equations are expressed respectively as follows:

$$\log(q_e - q_t) = \log q_e - \frac{k_1}{2.303} t \quad (4)$$

$$\frac{t}{q_t} = \frac{1}{k_2 q_e^2} + \frac{1}{q_e} t \quad (5)$$

where q_e and q_t (mg g^{-1}) are the adsorption capacities at equilibrium state and at time t (min), respectively, k_1 (min^{-1}) and k_2 (g mg^{-1} min^{-1}) are the rate constants, respectively. For the pseudo-first-order model, the values of k_1 and $q_{e,1}$ are calculated from the slope and intercept of plots of $\log(q_e - q_t)$ *versus* t (Fig. S6†). Similarly, for pseudo-second-order kinetic model, the values of k_2 and $q_{e,2}$ can be obtained by plots of t/q_t *versus* t, as shown in Fig. 6. The calculated kinetic parameters and the correlation coefficients (R^2) are listed in Table S1† and 1. Both of the correlation coefficients of pseudo-second-order kinetic (R_2^2) were even more near 1. The $q_{e,2}$ values were calculated to be 70.92 and 64.60 mg g^{-1} for samples MBH and MBA respectively. The experimental measured $q_{e,exp}$ values were 69.78 and 64.01 mg g^{-1} for samples MBH and MBA respectively. It can be

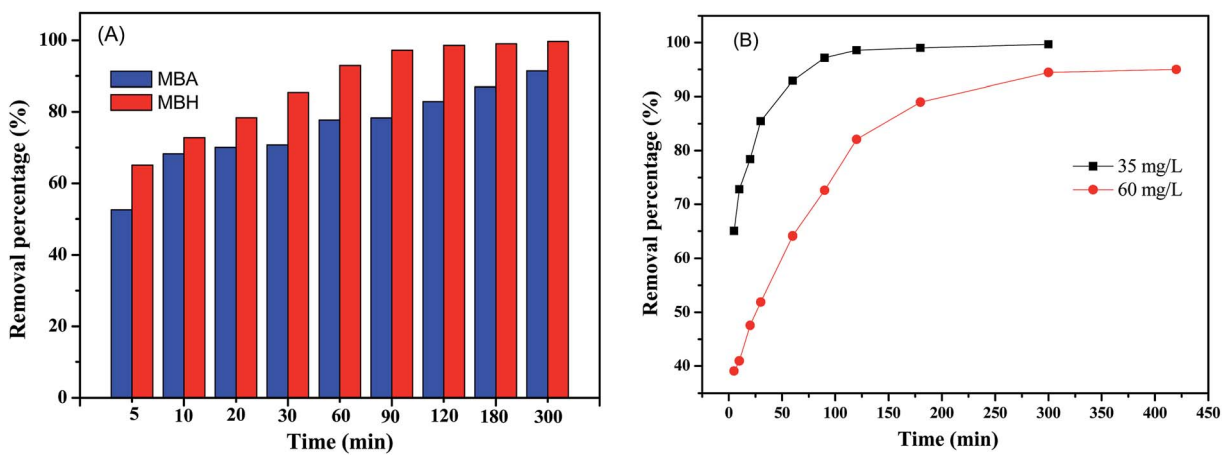

Fig. 5 Effect of contact time on CR removal efficiency by the 10 mg of prepared MBH and MBA nanostructures for 20 mL CR solution with initial concentrations of 35 mg L^{-1} (A); (B) the comparison of CR removal efficiency by the prepared MBH nanostructure for initial CR concentrations of 35 mg L^{-1} and 60 mg L^{-1}, keeping others conditions unchanged.

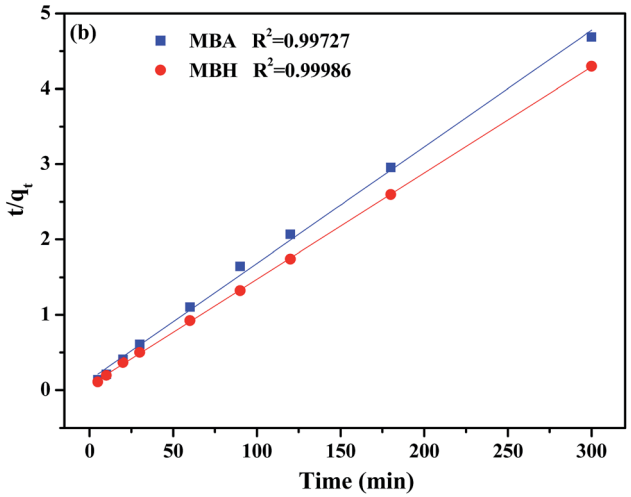

Fig. 6 Pseudo-second-order kinetic for adsorption of CR onto the MBH and MBA nanostructures.

Table 1 Pseudo-second-order kinetic constants of CR onto the MBH and MBA nanostructures

Samples	$q_{e,exp}$ (mg g^{-1})	$q_{e,cal}$ (mg g^{-1})	k_2 ($\times 10^{-3}$ g mg^{-1} min^{-1})	R_2^2
MBH	69.78	70.92	14.1	0.9973
MBA	64.01	64.60	1.80	0.9999

seen that the $q_{e,2}$ was close to $q_{e,exp}$, respectively. All these results indicated the pseudo-second-order kinetic model was more suitable for the description of adsorption of the MBH or MBA microspheres to CR, which implied that chemical adsorption was the main mechanism for the adsorption process.[23]

In order to elucidate the internal adsorption mechanism during the adsorption process and to investigate whether the intra particle diffusion in the adsorption process is a rate-limiting factor, we have further studied the adsorption kinetics data using the internal diffusion model. The empirical intra particle diffusion model is common to most adsorption processes,[24] which is expressed as eqn (6):

$$q_t = k_d\sqrt{t} + c \quad (6)$$

where k_d is the intra-particle diffusion rate constant (mg g^{-1} h$^{1/2}$), and c is the intercept of corresponding stages (mg g^{-1}), which represents the thickness of the boundary layer. The larger c means the greater contribution of the surface adsorption in the rate controlling step. When the $c = 0$, it indicates that film diffusion or boundary layer diffusion can be negligible, and the intra-particle diffusion becomes single rate controlling step. Fig. 7 presents the internal diffusion model curves of CR adsorption for samples MBH and MBA. The relevant diffusion parameters for each segment of linearization are shown in Table S2.† It can be seen from Fig. 7 that the model was not linear over the entire time range, but it existed a certain degree of linearity in stages, indicating that the entire adsorption process could be divided into several stages.[20] The first

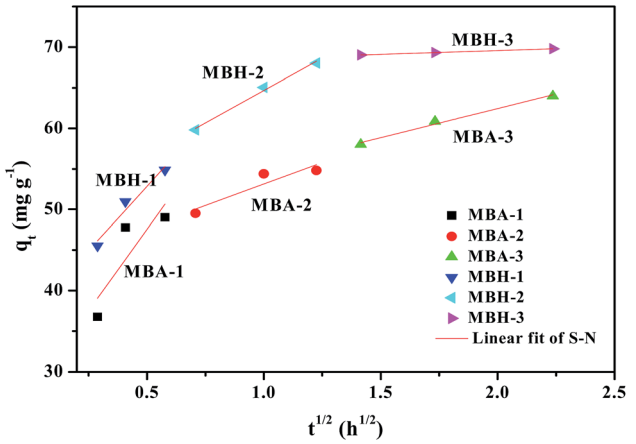

Fig. 7 Intra-particle diffusion model for CR adsorption on the samples MBH and MBA.

linear segment was the steepest, driven by the initial high concentration of CR difference, which could be regarded as the transfer of dye molecules from bulk solution to the microsphere surface or instantaneous adsorption. The second linear segment was the gradual adsorption phase, in which the intraparticle diffusion was the rate limiting steps. The third segment was relatively flat that was the final equilibrium phase, when the intra-particle diffusion became slow gradual, resulting in lower residual CR concentrations in the solution. The diffusion constant (K_d) gradually decreased from the first phase to the third phase, which indicates that CR adsorption is the fastest at the very beginning. If the intercept (c) in the internal diffusion model is 0, it means that the internal diffusion is the only speed control step.[20] Obviously, it can be seen that c is not zero from Table S2,† indicating that this adsorption process is mainly controlled by internal diffusion control. It is also found that K_d is decreasing while intercept c is increasing, indicating that the thickness of the boundary gradually increases and the adsorption rate decreases during the adsorption process. Therefore, the adsorption of CR by MBH or MBA may be determined by internal diffusion and surface adsorption.

Adsorption isotherms

Adsorption isotherms play a crucial role in predicting the mechanism of interaction between CR molecules and adsorbent surface active sites. The following Langmuir and Freundlich isotherm models are representative mathematical models that have been widely applied to study the adsorption mechanisms.[25] The Langmuir model (7) is proposed on an ideal homogeneous monolayer adsorption that the active sites on the adsorbent surface are equivalent and no interaction exists between the adsorbed contaminants, while the Freundlich model (8) is used for multilayer adsorption on heterogeneous surfaces.[23]

$$\frac{C_e}{q_e} = \frac{1}{K_L q_m} + \frac{C_e}{q_m} \quad (7)$$

$$\log q_e = \log K_F + \frac{1}{n}\log C_e \quad (8)$$

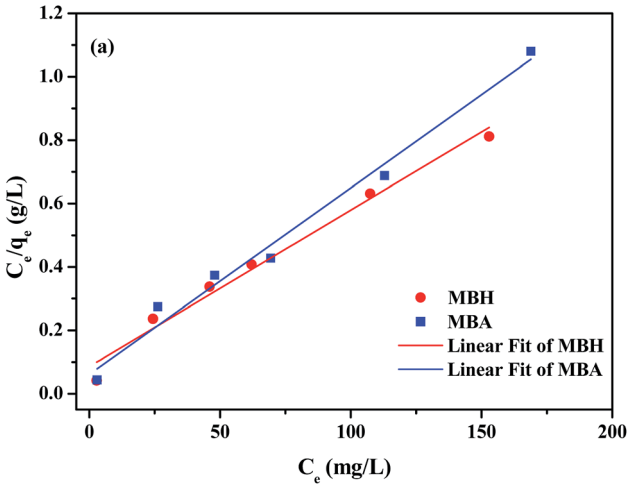

Fig. 8 Plot of C_e/q_e *versus* C_e for the CR adsorption by the MBH and MBA nanostructures fitting with the Langmuir isotherm adsorption model.

Table 2 Isotherm parameters for the adsorption of CR onto the MBH and MBA nanostructures

	Langmuir isotherm model			Freundlich isotherm model		
Adsorbent	q_m (mg g^{-1})	K_L (L mg^{-1})	R^2	K_F	n	R^2
MBH	202.84	0.0573	0.9793	50.26	3.86	0.9714
MBA	170.07	0.0957	0.9817	51.27	4.25	0.8857

The adsorption isotherms at different initial CR concentrations (20–200 mg L^{-1}) are shown in Fig. 8 and S7.† The parameters equilibrium constant K_L (L mg^{-1}) and Langmuir maximum adsorption capacity q_m (mg g^{-1}) can be calculated by the intercept and slope from the linear plot of C_e/q_e *versus* C_e (Fig. 8). In the same manner, the parameters K_F (roughly an indicator of the adsorption capacity) and n (adsorption intensity) can be confirmed through linear Freundlich isotherm model (Fig. S7†). Table 2 gives the values of related parameters and the correlation coefficients. Compared with the Freundlich model, the Langmuir model with the larger R^2 is more compatible with the experimental data, which indicates that the adsorption of adsorbent MBH or MBA may originate from the active sites uniformly distributed on the surface, and the adsorption is a monolayer adsorption for CR. From Table 2, it can be found that $0 < K_L < 1$, indicating that the adsorption process was preferential adsorption.[26]

The gained maximum adsorption capacities (q_m) of MBH and MBA were 202.84 and 170.07 mg g^{-1} respectively, which were much higher than most reported adsorbent materials as listed in Table 3. It can be predicted that the obtained MBH and MBA flower-like microsphere samples might be used as excellent and highly efficient adsorbent materials to remove and immobilize anionic organic contaminants from polluted wastewater.

Aiming at a realistic application, it would be important to understand the amounts of CR adsorbed by the prepared samples using tap and river water samples to prepare the CR solutions. As shown in following Fig. S8(A),† the removal percentage of CR for MBH sample was still very high compared with CR solutions prepared by using deionized water. It is also found that the CR solutions prepared by using river water has been adsorbed more quickly, as shown in Fig. S8(B)† for the UV-vis absorption spectra of CR solutions after being treated by the MBH nanostructures for 30 min. This more quick removal rate might be related with the micro-biological degradation in tap and river water samples.

Adsorption thermodynamics

In order to inspect the effects of temperature on adsorption and further study the adsorption mechanism, we also carried out

Table 3 Comparison of maximum adsorption capacity of MBH and MBA architectures with other adsorbents for removal of Congo red[a]

Adsorbents	q_m (mg g^{-1})	References
Montmorillonite (MMT)	12.7	27
Hierarchical urchin-like α-Fe_2O_3 nanostructures	66	28
γ-Al_2O_3/$Ni_{0.5}Zn_{0.5}Fe_2O_4$ microfibers	75.5	29
Hierarchical $Ni(OH)_2$ nanosheets	82.9	30
α-Fe_2O_3 hollow structures	93.55	31
Ca-bentonite	107.41	32
Dual-porosity Mn_2O_3 cubes	125.6	33
Hierarchical NiO nanosheets	151.7	30
Hollow nest-like α-Fe_2O_3 spheres	160	34
Hierarchical porous flower-like MBA microspheres	170.07	This work
Hierarchical porous MBO microspheres	183.15	15
Hierarchical porous flower-like MBH microspheres	202.84	This work
Hierarchical γ-AlOOH	214.59	35
$MgBO_2(OH)$ superstructures	228.3	14
γ-Al_2O_3 microspheres	416.05	35
Functionalized carbon nanotube/mixed metal oxides	1250	36
Monodispersed hierarchical flower-like nickel(II) oxide	534.8	37
Hierarchically porous SiO_2/C hollow microspheres	2512	38

[a] All the maximum adsorption capacities were obtained by fitting the equilibrium adsorption data for a series of different concentrations in the Langmuir model.

Table 4 Thermodynamic parameters for CR adsorption by MBH and MBA nanostructures

Adsorbent	T (K)	ΔG^0 (kJ mol^{-1})	ΔH^0 (kJ mol^{-1})	ΔS^0 (kJ mol^{-1} K^{-1})
MBH	293	−7.912	110.2	0.4027
	298	−9.613		
	303	−11.95		
MBA	293	−5.510	80.92	0.2947
	298	−6.724		
	303	−8.462		

the investigation of adsorption thermodynamics. The Gibbs free energy change ΔG^0 related with the adsorption process can be obtained by equilibrium constant K_d through the classical Van't Hoff equations (eqn (9) and (10)).

$$\Delta G^0 = -\mathrm{RT} \ln K_d \quad (9)$$

$$\ln K_d = -\frac{\Delta H^0}{\mathrm{RT}} + \frac{\Delta S^0}{R} \quad (10)$$

$$K_d = \frac{q_e}{C_e} \quad (11)$$

where q_e and C_e are the adsorption capacity and concentration of the CR at equilibrium state.

The entropy change (ΔS^0) and enthalpy change (ΔH^0) can be obtained through intercept and slope of $\ln K_d$ *versus* $1/T$, as shown in Fig. S9.† The Gibbs free energy (ΔG^0) at the corresponding temperature can be calculated according eqn (9). The above thermodynamic parameters are all listed in Table 4.

The value of ΔG^0 is negative, indicating that the adsorption of CR by sample MBH or MBA is a spontaneous process, and the increase of temperature is favorable for the adsorption. The positive value of ΔH^0 reveals that the adsorption is endothermic reaction, which indicates that the adsorption process is chemical adsorption.[39] The positive value of ΔS^0 indicates the randomness is increased during the adsorption of CR on MBH and MBA microspheres.

Conclusions

In summary, highly uniform nanosheets constructed $7MgO{\cdot}2B_2O_3{\cdot}7H_2O$ (MBH) and $3MgO{\cdot}B_2O_3$ (MBA and MBB) microspheres with hierarchical porous architecture had been successfully fabricated *via* a mild phase transformation and thermal conversion method, respectively. This continuous preparation strategy is simple and green, and the corresponding growth mechanisms were also proposed. Moreover, MBH and MBA microspheres had a specific selectivity for the adsorption of CR, with the maximum adsorption capacities of 202.84 mg g^{-1} and 170.07 mg g^{-1}, respectively. The excellent adsorption performances of MBH and MBA for CR were attributed to the synergistic effect of the more surface positive charge, larger specific surface area and more active sites. The adsorptions of CR on the two prepared adsorbents were fitted with the pseudo-second-order kinetics model, and satisfied well with the Langmuir model. Meanwhile, the result for the investigation of adsorptive thermodynamics showed that the adsorption process was a spontaneous and endothermic process. It can be predicated that both hierarchical porous microsphere samples could be as promising candidates for immobilized CR dye pollutant from wastewater because of their economics, excellent adsorption capacity and environmentally friendly.

Conflicts of interest

There are no conflicts to declare.

Acknowledgements

This project is supported by the National Natural Science Foundation of China (No. 21573142).

References

1 R. M. Yu, Y. Z. Shi, D. Z. Yang, Y. X. Liu, J. Qu and Z. Z. Yu, *ACS Appl. Mater. Interfaces*, 2017, **9**, 21809–21819.
2 F. Chen, A. S. Gong, M. Zhu, G. Chen, S. D. Lacey, F. Jiang, Y. Li, Y. Wang, J. Dai, Y. Yao, J. Song, B. Liu, K. Fu, S. Das and L. Hu, *ACS Nano*, 2017, **11**, 4275–4282.
3 Y. Q. Zheng, B. C. Zhu, H. Chen, W. You, C. J. Jiang and J. G. Yu, *J. Colloid Interface Sci.*, 2017, **504**, 688–696.
4 S. Vahidhabanu, A. A. Idowu, D. Karuppasamy, B. R. Babu and M. Vineetha, *ACS Sustainable Chem. Eng.*, 2017, **5**, 10361–10370.
5 L. S. Zhong, J. S. Hu, H. P. Liang, A. M. Cao, W. G. Song and L. J. Wan, *Adv. Mater.*, 2006, **18**, 2426–2431.
6 M. A. Mudassir, S. Z. Hussain, A. Rehman, W. Zaheer, S. T. Asma, A. Jilani, M. Aslam, H. Zhang, T. M. Ansari and I. Hussain, *ACS Appl. Mater. Interfaces*, 2017, **9**, 24190–24197.
7 C. J. Pei, G. P. Han, Y. Zhao, H. Zhao, B. Liu, L. J. Cheng, H. Q. Yang and S. Z. Liu, *J. Hazard. Mater.*, 2016, **318**, 732–741.
8 Y. Q. Zhang, X. B. Yang, Z. X. Wang, J. Long and L. Shao, *J. Mater. Chem. A*, 2017, **5**, 7316–7325.
9 Y. Zeng, H. B. Yang, W. Y. Fu, L. Qiao, L. X. Chang, J. J. Chen, H. Y. Zhu, M. H. Li and G. T. Zou, *Mater. Res. Bull.*, 2008, **43**, 2239–2247.
10 L. Zhang and Z. H. Liu, *J. Therm. Anal. Calorim.*, 2017, **129**, 715–719.
11 W. Zhu, R. Wang, S. Zhu, L. Zhang, X. Cui, H. Zhang, X. Piao and Q. Zhang, *ACS Sustainable Chem. Eng.*, 2014, **2**, 836–845.
12 W. C. Zhu, S. L. Zhu and L. Xiang, *CrystEngComm*, 2009, **11**, 1910–1919.
13 A. M. Chen, J. Li, P. Gu and J. Hu, *Powder Technol.*, 2014, **267**, 54–60.
14 Z. Q. Zhang, W. C. Zhu, R. G. Wang, L. L. Zhang, L. Zhu and Q. Zhang, *J. Mater. Chem. A*, 2014, **2**, 19167–19179.
15 Y. Q. Ma and Z. H. Liu, *J. Taiwan Inst. Chem. Eng.*, 2018, **86**, 92–100.
16 S. Y. Gao, Z. G. Chen and J. N. Feng, *Chin. J. Inorg. Chem.*, 1986, **1–2**, 40–52.

17 W. Li, S. Y. Gao, S. P. Xia, V. M. Valyashko and M. A. Urusova, *Thermochim. Acta*, 1998, **308**, 183–188.
18 J. Li, S. P. Xia and S. Y. Gao, *Spectrochim. Acta. A.*, 1995, **51**, 519–532.
19 J. B. Condon, *Surface area and porosity determinations by physisorption: measurements and theory*, Elsevier, Amsterdam, 2006.
20 D. Maiti, S. Mukhopadhyay and P. S. Devi, *ACS Sustainable Chem. Eng.*, 2017, **5**, 11255–11267.
21 R. Yu, Y. Shi, D. Yang, Y. Liu, J. Qu and Z. Z. Yu, *ACS Appl. Mater. Interfaces*, 2017, **9**, 21809–21819.
22 J. L. Marco-Brown, L. Guz, M. S. Olivelli, B. Schampera, R. M. Torres Sánchez, G. Curutchet and R. Candal, *Chem. Eng. J.*, 2018, **333**, 495–504.
23 H. Qian, Y. L. Lin, B. Xu, L. P. Wang, Z. C. Gao and N. Y. Gao, *Chem. Eng. J.*, 2018, **349**, 849–859.
24 J. S. Wu, J. S. Wang, H. Y. Li, Y. C. Du, K. L. Huang and B. X. Liu, *J. Mater. Chem. A*, 2013, **1**, 9837–9847.
25 A. Afkhami and R. Moosavi, *J. Hazard. Mater.*, 2010, **174**, 398–403.
26 Z. Huang, Y. Li, W. Chen, J. Shi, N. Zhang, X. Wang, Z. Li, L. Gao and Y. Zhang, *Mater. Chem. Phys.*, 2017, **202**, 266–276.
27 L. Wang and A. Q. Wang, *J. Hazard. Mater.*, 2007, **147**, 979–985.
28 J. Fei, Y. Cui, J. Zhao, L. Gao, Y. Yang and J. Li, *J. Mater. Chem.*, 2011, **21**, 11742–11746.
29 X. C. Yang, Z. Wang, M. X. Jing, R. J. Liu, L. Jin and X. Q. Shen, *Water, Air, Soil Pollut.*, 2014, **225**, 1819–1830.
30 B. Cheng, Y. Le, W. Q. Cai and J. G. Yu, *J. Hazard. Mater.*, 2011, **185**, 889–897.
31 J. Wu, J. Wang, H. Li, Y. Du, K. Huang and B. Liu, *J. Mater. Chem. A*, 2013, **1**, 9837–9847.
32 L. L. Lian, L. P. Guo and C. J. Guo, *J. Hazard. Mater.*, 2009, **161**, 126–131.
33 Y. J. Shao, B. Ren, H. M. Jiang, B. J. Zhou, L. P. Lv, J. Z. Ren, L. C. Dong, J. Li and Z. F. Liu, *J. Hazard. Mater.*, 2017, **333**, 222–231.
34 Z. H. Wei, R. E. Xing, X. Zhang, S. Liu, H. H. Yu and P. C. Li, *ACS Appl. Mater. Interfaces*, 2012, **5**, 598–604.
35 Z. F. Li, Y. Du, S. Y. Zhang, Z. T. Chen, K. Yang, X. J. Lv and C. F. Zhua, *RSC Adv.*, 2016, **6**, 89699–89707.
36 S. X. Yang, L. Y. Wang, X. D. Zhang, W. J. Yang and G. L. Song, *Chem. Eng. J.*, 2015, **275**, 315–321.
37 Y. Q. Zheng, B. C. Zhu, H. Chen, W. You, C. J. Jiang and J. G. Yu, *J. Colloid Interface Sci.*, 2017, **504**, 688–696.
38 J. Wang, L. Y. Xiao, S. A. Wen, N. Chen, Z. Y. Dai, J. Y. Deng, L. H. Nie and J. Min, *RSC Adv.*, 2018, **8**, 19852–19860.
39 S. H. Kim and P. P. Choi, *Dalton Trans.*, 2017, **46**, 15470–15479.